Magnetic Domain Pattern and Characteristic Deterioration of Electrical Steel Due to Laser Cutting

Rawal Shahbaz[1,2], Changgeng Zhang[1,2], Hina Fatima[3], Raja Saqib Arshad[1,2], and Sujun Babu[1,2]

[1]State Key Laboratory of Smart Power Distribution Equipment and System, Hebei University of Technology, Tianjin 300130, China

[2]Hebei Key Laboratory of Equipment and Technology Demonstration of Flexible DC Transmission, Hebei University of Technology, Tianjin 300130, China

[3]Department of Optical Information Science and Technology, School of Physics, Xidian University, Xi'an 710071, China

Nonoriented electrical steel (NOES) is the cornerstone soft magnetic material for transformer cores and motor laminations, yet laser cutting degrades magnetic performance through localized thermal damage that fundamentally alters domain microstructure and wall dynamics. While prior studies qualitatively documented domain distortion near cut edges, quantitative methods linking microscopic domain evolution to macroscopic hysteresis remain limited. This study systematically quantifies laser cutting-induced magnetic domain reconfiguration in grade 35WW250 NOES using a NanoMOKE3 scanning magneto-optical Kerr effect (MOKE) magnetometer across a 2–12 mm spatial gradient in longitudinal and transverse geometries. A principal methodological innovation is the application of the seven invariant Hu moment set and principal component analysis (PCA) to categorize domain morphology into $K = 4$ distinct clusters, capturing >87% of morphological variance, providing a framework for estimating macroscopic hysteresis loops through weighted averaging of local magneto-optical responses. Results reveal severe spatial degradation: coercivity increased 206% (222–678 A/m) and the reconstructed hysteresis component of core loss nearly doubled (13 674–27 704 W/m^3 at 50 Hz, 1.0 T) within 2 mm of the cut edge, driven by domain wall rigidification and staircase-type hysteresis from intensified pinning. The domain wall pinning coefficient rose 3.18-fold (250–795 A/m) while initial permeability collapsed 5.6-fold. A physically significant crossover field $H^* \approx$ 989 A/m is identified, below which rigid cut-edge walls dissipate less energy than the undamaged interior. All parameters recovered to within 4%–8% of reference values at 12 mm, defining a ~10.6 mm practical damage zone.

***Index Terms*—Core loss, Hu moment invariants, laser cutting, magnetic degradation, magnetic domain dynamics, magnetization curves, magneto-optical Kerr effect (MOKE), nonoriented electrical steel (NOES).**

NOMENCLATURE

$\boldsymbol{H}$	Applied magnetic field	A/m or Oe.
$\boldsymbol{H_{max}}$	Maximum applied field amplitude	A/m or Oe.
$(\boldsymbol{H_c})$	Coercive field	A/m or Oe.
$(\boldsymbol{H^*})$	Model-based crossover field	A/m or Oe.
$(\boldsymbol{M})$	Magnetization	A/m or normalized.
$(\boldsymbol{M_s})$	Saturation magnetization	A/m.
$(\boldsymbol{M_{an}})$	Anhysteretic magnetization	A/m.
$(\boldsymbol{M_{irr}})$	Irreversible magnetization	A/m
$(\boldsymbol{M_{rev}})$	Reversible magnetization	A/m.
$(\boldsymbol{B})$	Magnetic flux density	T.
$(\boldsymbol{B_m})$	Peak magnetic flux density	T.
$(\boldsymbol{B_r})$	Remanent flux density	T or normalized.
$(\boldsymbol{x})$	Distance from laser-cut edge	mm.
$(\boldsymbol{W})$	Energy dissipated per hysteresis cycle	J/m^3 or relative loop area.
$(\boldsymbol{R(H)})$	Damage ratio, (W_{edge}/W_{center})	Dimensionless.
(μ_i)	Initial permeability	Dimensionless or H/m.
(χ_i)	Initial susceptibility	Dimensionless.
(α_R)	Rayleigh coefficient	Depending on formulation.
(α_{JA})	Jiles–Atherton mean-field coupling parameter	Dimensionless.
$(\boldsymbol{k_{JA}})$	Jiles–Atherton pinning parameter	A/m.
$(\boldsymbol{a})$	Jiles–Atherton anhysteretic shape parameter	A/m.
$(\boldsymbol{c})$	Jiles–Atherton reversibility coefficient	Dimensionless.
$(\boldsymbol{P})$	Estimated magnetic loss	W/m^3 or W/kg.

Received 28 March 2026; revised 26 May 2026; accepted 30 June 2026. Date of publication 8 July 2026; date of current version 27 August 2026. Corresponding author: C. Zhang (e-mail: changgeng.zhang@hebut.edu.cn).

Color versions of one or more figures in this article are available at https://doi.org/10.1109/TMAG.2026.3711353.

Digital Object Identifier 10.1109/TMAG.2026.3711353

0018-9464 © 2026 IEEE. All rights reserved, including rights for text and data mining, and training of artificial intelligence and similar technologies. Personal use is permitted, but republication/redistribution requires IEEE permission.
See https://www.ieee.org/publications/rights/index.html for more information.

Authorized licensed use limited to: Hebei University of Technology. Downloaded on November 12,2026 at 05:41:56 UTC from IEEE Xplore. Restrictions apply.

(P_h)	Hysteresis loss component	W/m^3 or W/kg
(P_e)	Eddy-current loss component	W/m^3 or W/kg.
(P_{ex})	Excess loss component	W/m^3 or W/kg.
(f)	Excitation frequency	Hz.
(k_h)	Hysteresis-loss coefficient	Model-dependent.
(ke)	Eddy-current loss coefficient	Model-dependent.
(kex)	Excess-loss coefficient	Model-dependent.
(β, β_c)	Spatial decay constants	mm^{-1}.
(Ii)	(i)th Hu moment invariant	Dimensionless.
$(\hat{I}_i)$	Log-transformed Hu moment invariant	Dimensionless.
(K)	Number of K-means clusters	Dimensionless.
(Ai)	Areal fraction of cluster (j)	Dimensionless.
LD	Longitudinal MOKE geometry	—.
TD	Transverse MOKE. geometry	—
HAZ	Heat-affected zone	—.

I. Introduction

NONORIENTED electrical steel (NOES) is the principal soft magnetic material for transformer cores, motor laminations, and generator stators, where magnetic properties directly govern energy conversion efficiency and operational stability [1], [2]. As global energy demand intensifies and efficiency standards tighten, exemplified by IEC60034-30-1 for motors and EN 50588 for transformers, minimizing core loss in NOES components has become a critical engineering imperative [3], [4].

Laser cutting has emerged as the dominant precision-forming technique for NOES owing to its noncontact nature, high dimensional accuracy ($\pm$0.05 mm), and compatibility with complex geometries [5], [6]. However, the high energy density of the laser beam generates steep thermal gradients at the cut interface, inducing localized melting, rapid solidification, residual stress accumulation, and microstructural modification. These thermally mediated effects degrade magnetic properties, manifesting as increased coercivity, elevated hysteresis loss, and reduced permeability, thereby partially negating the efficiency advantages motivating NOES adoption in precision electromagnetic devices [7], [8].

Prior investigations have predominantly employed macroscopic characterization techniques, including vibrating sample magnetometry (VSM) and Epstein frame measurements, to quantify the influence of processing parameters on bulk metrics such as core loss per unit mass [9], [10]. While establishing that damage concentrates within a few millimeters of the cut edge, these studies provide limited insight into microscopic domain-level mechanisms. Scanning magneto-optical Kerr effect (MOKE) magnetometry offers submicrometer spatial resolution for in situ domain observation; however, its application to laser-cut NOES has been largely qualitative [11], [12]. Three critical gaps persist: 1) the absence of high-precision quantitative methods for extracting morphological features from domain images; 2) the lack of a validated methodology for reconstructing macroscopic hysteresis loops from microscopic domain information; and 3) insufficient systematic characterization of domain behavior along both longitudinal and transverse directions (TDs) under variable external fields, limiting understanding of the spatial degradation gradient [13].

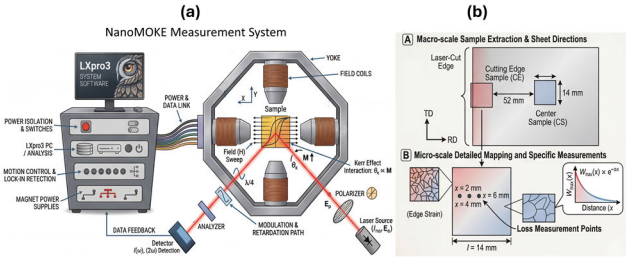


Fig. 1. Experimental configuration and spatial measurement scheme. (a) Schematic of the NanoMOKE3 measurement system used to acquire local longitudinal and transverse MOKE hysteresis loops. (b) Definition of the sample geometry and measurement positions. For the laser-cut edge sample, $x = 0$ is located at the laser-cut boundary, and MOKE measurements were performed at selected distances x from the edge toward the sheet interior. The center sample was measured at six reference positions to evaluate natural local magnetic variability in the undamaged sheet region.

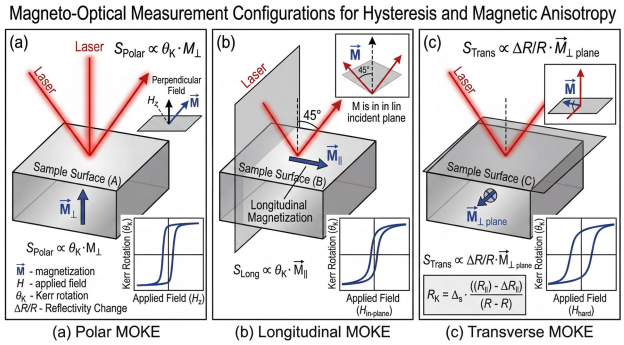


Fig. 2. Three basic configurations of MOKE. (a) Polar, (b) longitudinal, and (c) transverse, along a magnetization vector corresponds to the sensitivity axis.

This study presents a comprehensive experimental investigation of laser cutting-induced magnetic domain reconfiguration in grade 35WW250 NOES. The primary objectives are: 1) to characterize the spatial evolution of domain structure and hysteresis morphology from the cut edge to the sheet center using NanoMOKE3 MOKE magnetometry; 2) to introduce Hu moment invariants as quantitative descriptors of domain image features, enabling statistically robust cross-position comparison; and 3) to establish mechanistic and quantitative correlations between laser-induced thermal damage, microscopic domain reorganization, and macroscopic magnetic degradation through analytical modeling.

II. Material and Methodology

A. Material and Sample Preparation

The material investigated was commercial-grade 35WW250 nonoriented silicon steel (WISCO, China) with a nominal thickness of 0.35 mm [14]. Bulk magnetic properties include a

Authorized licensed use limited to: Hebei University of Technology. Downloaded on November 12,2026 at 03:41:56 UTC from IEEE Xplore. Restrictions apply.

maximum core loss of 2.50 W/kg (at 1.5 T, 50 Hz) and a mass density of approximately 7650 kg/m^3. In-plane magnetization dynamics were resolved across a 2–12 mm gradient using a NanoMOKE3 magnetometer (λ = 635 nm, spot size $\approx$ 2 μm), as illustrated in Fig. 1(a).

Two 14 × 14 mm^2 specimens were prepared from the same sheet. Sample 1, the undamaged reference, was extracted from the geometric center by wire electrical discharge machining. For Sample 2, one edge coincided with the industrial laser cut edge [Fig. 1(b)], and the spatial coordinate x was defined from this boundary (x = 0 at the edge, increasing inward). MOKE measurements were performed at x = 2, 4, 6, 8, 10, and 12 mm, all within the specimen, with the 12 mm point 2 mm from the opposite edge. The cut was produced using a 1.5 kW fiber laser at 30 m/min with a verified kerf width of 0.2 mm.

B. NanoMOKE3 Measurement Configuration

The NanoMOKE system operated in longitudinal direction (LD) and transverse (TD) configurations as shown in Fig. 2. LD-MOKE captures the in-plane magnetization component parallel to the plane of incidence ($M_{\parallel}$) via Kerr rotation (θ_K), whereas TD-MOKE resolves the perpendicular component ($M_{\perp}$) through reflectivity modulation ($\Delta R/R$). These orthogonal configurations probe distinct magnetooptical mechanisms: polarization rotation in one case and intensity change in the other. The resulting complementary hysteresis information is required to fully characterize inplane magnetic anisotropy. The normalized local magnetization is given by

$$m(x,H) = S_{MOKE}(x,H)/S_{sat} \tag{1}$$

where $m(H)$ is the normalized local magnetization obtained from the MOKE signal at applied magnetic field H. S (x, H) is Kerr intensity at field H measured at multiple distances x and S_{sat} is the saturated Kerr signal.

Scanning was performed at a 1 μm step size with a 0.1 Hz quasi-static field sweep, averaged over 300 cycles to optimize the signal-to-noise ratio.

C. Magnetic-Parameter Extraction and Model-Based Analysis

The local MOKE hysteresis loops were used to extract the main magnetic parameters, including coercivity H_c, remanence B_r, initial permeability μ_i, and relative hysteresis-loop area. The coercive field H_c was obtained from the field value where the normalized magnetization crosses zero. The remanence B_r was estimated from the normalized magnetization at H = 0, and the initial permeability μ_i was calculated from the low-field slope of the magnetization curve near the origin. These parameters were extracted separately for the longitudinal and transverse MOKE loops.

For the low-field region, the Rayleigh model [15] was used to describe the initial magnetization response

$$M(H) = \chi_i H + \alpha_R H^2 \tag{2}$$

where $M(H)$ is the magnetization at applied field H, χ_i is the initial susceptibility, and α_R is the Rayleigh coefficient. The first term represents the reversible low-field response, while the second term represents the irreversible contribution from small domain-wall [16] displacements.

The corresponding Rayleigh hysteresis branches are expressed as

$$M(H) = (\chi_i + \alpha_R H_m)H \pm \frac{\alpha_R}{2}\left(H^2 - H_m^2\right) \tag{3}$$

where H_m is the maximum field amplitude during the cycle. The signs + and − correspond to the increasing-field and decreasing-field branches, respectively. The Rayleigh coefficient α_R was used as a low-field indicator of irreversible domain-wall displacement.

To further quantify laser-induced pinning, the measured loops were fit using the Jiles–Atherton model [17]. The total magnetization was considered as the sum of reversible and irreversible magnetization components. The differential form used in this study is

$$\frac{dM}{dH} = (1-c)\frac{M_{\text{an}} - M_{\text{irr}}}{k_{\text{JA}}\delta - \alpha_{\text{JA}}(M_{\text{an}} - M_{\text{irr}})} + c\frac{dM_{\text{an}}}{dH} \tag{4}$$

where M is the total magnetization, M_{irr} is the irreversible magnetization, and M_{an} is the anhysteretic magnetization. M_{an} was calculated using the Langevin function [18]. c is the reversibility coefficient, δ is the field-direction parameter, α_{JA} is the inter-domain coupling parameter, and k_{JA} is the Jiles–Atherton pinning parameter. In this work, k_{JA} was used as an effective indicator of the energy barrier opposing irreversible domain wall motion.

The spatial recovery of coercivity away from the laser-cut edge was fit using an exponential decay function

$$H_c(x) = H_{c,\infty} + (H_{c,0} - H_{c,\infty})e^{-\beta_c x} \tag{5}$$

where $H_c(x)$ is the coercive field at distance x from the laser-cut edge, $H_{c,\infty}$ is the reference coercivity far from the cut edge, $H_{c,0}$ is the extrapolated coercivity at the cut interface, and β_c is the spatial decay constant. The characteristic recovery length is given by $1/\beta_c$.

The local magnetic loss was estimated using a three-component Steinmetz/Bertotti-type expression

$$P(B,x) = K_h(B,x)B^{\gamma}f + K_e B^2 f^2 + K_{\text{ex}} B^{1.5} f^{1.5} \tag{6}$$

where $P(B, x)$ is the estimated magnetic loss, B is the magnetic flux density, f is the excitation frequency, and γ is the Steinmetz exponent. K_h, K_e, and K_{ex} are the hysteresis-loss, classical eddy current-loss, and excess-loss coefficients, respectively. Since the present measurements are based on local MOKE hysteresis loops, the calculated loss values were treated as relative local hysteresis loss estimates rather than direct bulk Epstein-frame core loss measurements.

The spatial variation of the hysteresis loss coefficient was described as

$$K_h(x) = K_{h,\infty} + (K_{h,0} - K_{h,\infty})e^{-\beta x} \tag{7}$$

where $K_h(x)$ is the distance-dependent hysteresis-loss coefficient, $K_{h,\infty}$ is the reference value far from the cut edge, $K_{h,0}$ is the extrapolated value at the cut interface, and β is the spatial decay constant. The fit parameters obtained from (5) and (7) are reported in the Results section.

Authorized licensed use limited to: Hebei University of Technology. Downloaded on November 12,2026 at 08:41:58 UTC from IEEE Xplore. Restrictions apply.

D. Image Processing and Hu-Moment Invariants

Raw intensity maps $f(x,y)$ were binarized using Otsu's method and segmented into discrete domain objects via eight-connectivity labeling. x and y are the horizontal and vertical pixel coordinates, respectively. For each domain, discrete raw moments $m_{pq} = \sum\sum x^p y^q f(x,y)$ where p and q are nonnegative integers describing the moment order and translationally invariant central image moments μ_{pq} were computed. These served as the basis for the seven Hu-moment invariants ($\Phi_1 - \Phi_7$), which provide a rotational and scale-invariant description of domain morphology, (8), as shown at the bottom of the page, where η_{pq} normalized central moment.

E. Morphological Clustering and Loop Reconstruction

The log-transformed Hu moment features were standardized using z-score normalization and subjected to principal component analysis (PCA) before K-means clustering with K = 4, chosen to separate the dominant domain patterns observed in the reference and laser-cut edge regions (elongated bulk-like domains versus fragmented pinned structures).

To connect domain morphology with the local magnetic response, the reconstructed magnetization loop was estimated as an area-weighted combination of representative local loops

$$\langle M_{rec}(H)\rangle = \frac{\sum_{i=1}^{K} A_i M_i(H)}{\sum_{i=1}^{K} A_i} \tag{9}$$

where $M_{rec}(H)$ is the reconstructed magnetization response as a function of applied magnetic field H. K is the total number of domain morphology clusters. A_i is the areal fraction of the ith cluster, and $M_i(H)$ is the representative hysteresis loop associated with that cluster. Since the area fractions are normalized, $\sum_{i=1}^{K} A_i = 1$, (9) represents the weighted average of local magnetic responses from different domain-morphology classes.

This reconstruction provides a compact link between image-based morphology and the measured MOKE response, supporting the interpretation of how domain structure changes contribute to magnetic degradation, while the directly measured MOKE loops remain the primary experimental data.

III. Results

A. Evaluation of Magnetization Curves

Figs. 3 and 4 compare the local MOKE hysteresis loops of the center reference sample and the laser-cut edge sample.

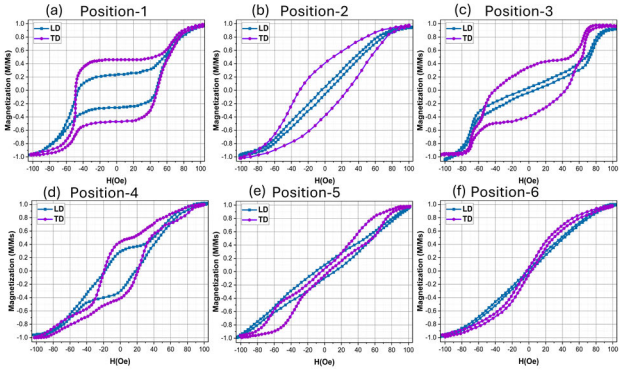


Fig. 3. (a)–(f) Magnetization curves of *sample-1*, which were extracted from the center of a silicon steel sheet; the observed six locations measured on Sample 1 represent repeated reference positions used to quantify natural spatial variability caused by grain texture and local anisotropy in both the longitudinal and TDs.

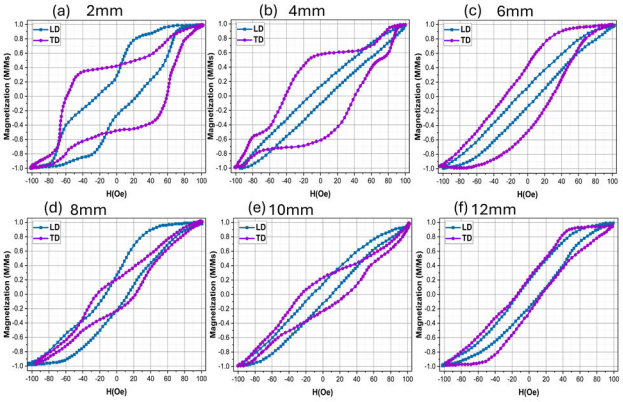


Fig. 4. (a)–(f) Magnetization curves for sample-2, which were extracted near the cutting edge of a silicon steel sheet, were observed at multiple points ranging from 2 to 12 mm in both the longitudinal and TDs.

The purpose of this comparison is first to establish the natural variability of the undamaged material and then to identify the additional distance-dependent degradation caused by laser cutting.

Fig. 3 shows the LD and TD loops measured at six reference positions in Sample 1. These loops at positions Fig. 3(a)–(f) were not interpreted as a distance-dependent laser-damaged specimen; instead, it was used as a bulk reference specimen extracted from the central region of the same sheet. The six locations measured on Sample 1 represent repeated reference positions used to quantify natural spatial variability caused by grain texture and local anisotropy. Local MOKE measurements

$$\begin{aligned}
\phi_1 &= \eta_{20} + \eta_{02} \\
\phi_2 &= (\eta_{20} - \eta_{02})^2 + 4\eta_{11}^2 \\
\phi_3 &= (\eta_{30} - 3\eta_{12})^2 + (3\eta_{21} - \eta_{03})^2 \\
\phi_4 &= (\eta_{30} + \eta_{12})^2 + (\eta_{21} + \eta_{03})^2 \\
\phi_5 &= (\eta_{30} - 3\eta_{12})(\eta_{30} + \eta_{12})\left[(\eta_{30} + \eta_{12})^2 - 3(\eta_{21} + \eta_{03})^2\right] + (3\eta_{21} - \eta_{03})(\eta_{21} + \eta_{03})\left[3(\eta_{30} + \eta_{12})^2 - (\eta_{21} + \eta_{03})^2\right] \\
\phi_6 &= (\eta_{20} - \eta_{02})\left[(\eta_{30} + \eta_{12})^2 - (\eta_{21} + \eta_{03})^2\right] + 4\eta_{11}(\eta_{30} + \eta_{12})(\eta_{21} + \eta_{03}) \\
\phi_7 &= (3\eta_{21} - \eta_{03})(\eta_{30} + \eta_{12})\left[(\eta_{30} + \eta_{12})^2 - 3(\eta_{21} + \eta_{03})^2\right] - (\eta_{30} - 3\eta_{12})(\eta_{21} + \eta_{03})\left[3(\eta_{30} + \eta_{12})^2 - (\eta_{21} + \eta_{03})^2\right]
\end{aligned} \tag{8}$$

Authorized licensed use limited to: Hebei University of Technology. Downloaded on November 12,2026 at 05:41:56 UTC from IEEE Xplore. Restrictions apply.

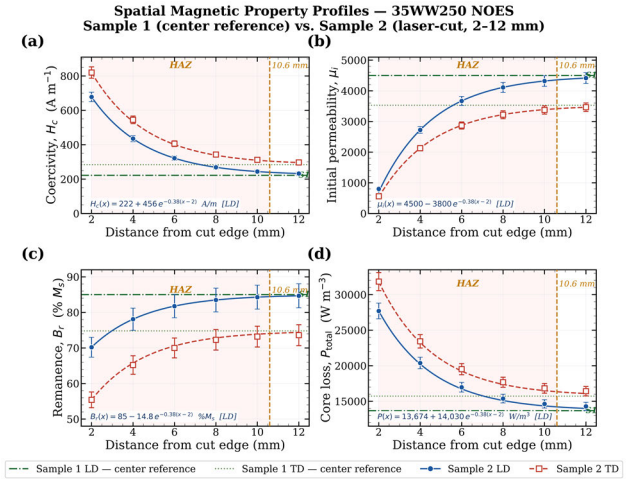


Fig. 5. Spatial magnetic property profiles (2–12 mm) for laser-cut 35WW250 NOES compared to Sample 1 reference. (a) Coercivity H_c follows exponential decay (5), (b) initial permeability μ_i illustrates severe HAZ suppression, (c) remanence B indicates domain fragmentation, and (d) total core loss P_{total} reflects intensified hysteresis loss near the cut. Vertical dashed lines mark the 10.6 mm damage boundary. Solid/dashed lines denote LD/TD geometry.

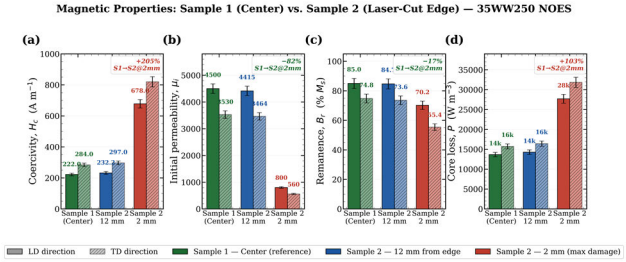


Fig. 6. Comparative analysis of magnetic properties for Sample 1 (center) and Sample 2 (12 and 2 mm from the edge) in LD and TD orientations. (a) Coercivity H_c shows a + 206% peak elevation, (b) initial permeability μ_i reveals an 82% reduction, (c) remanence B_r indicates a 17% drop, and (d) total core loss P reflects a 103% increase at the 2 mm position.

were performed at six nominal distances, $x = 2, 4, 6, 8, 10,$ and 12mm, measured from the original laser-cut boundary. Therefore, x denotes distance from the laser-cut edge only for Sample 2, whereas the corresponding positions in Sample 1 are reference measurement locations.

Fig. 4 shows the LD and TD loops measured in Sample 2 at $x = 2, 4, 6, 8, 10,$ and 12mm from the laser-cut edge. At $x = 2 - 4$mm, the loops show strong shearing, lower slope, and wider opening, indicating restricted domain-wall motion near the laser-affected edge. From $x = 6$ to 12 mm, the loops gradually recover toward the reference behavior, although a small LD/TD separation remains. This confirms that the degradation is strongest near the cut edge and weakens with distance.

B. Spatial Variation of Extracted Magnetic Parameters

The magnetic parameters extracted from the loops are summarized in Figs. 5 and 6. At $x = 2$ mm, the coercivity H_c reaches 678 A/m, compared with the center-reference value of 222 A/m, corresponding to a 206% increase. The fit spatial decay follows (5) with $H_{c,\infty} = 222$ A/m, $H_{c,0} = 1200$ A/m, and $\beta_c = 0.38$ mm^{-1}. The characteristic decay length is therefore approximately $1/\beta_c = 2.6$ mm. Degradation is further reflected in a 5.6-fold reduction in initial permeability, a 17%

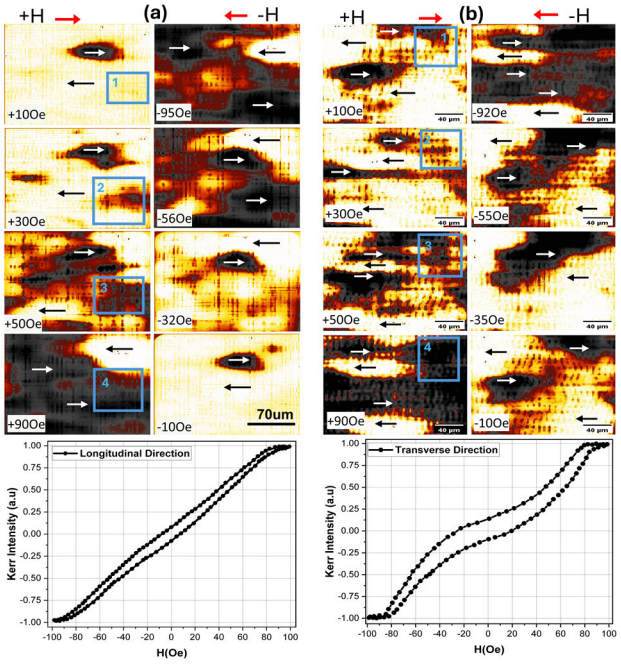


Fig. 7. Domain structure at the center of the sheet (Sample 1). (a) External applied field ±H in the LD and (b) external applied field ±H in the TD (ImageJ rendering).

reduction in remanence (TD geometry), and a 103% increase in estimated local hysteresis loss near the edge, calculated using the three-component Steinmetz-type expression (Section II-C). By 12 mm from the cut interface, all parameters recover to at least 91% of the undamaged reference values.

The spatial impact of laser cutting is captured solely by the hysteresis coefficient K_h, in (7), decaying exponentially from $k_{h,0} = 600$ at the cut edge to $k_{h,\infty} = 250$ (undamaged) with $\beta = 0.38$ mm^{-1}. Eddy current $K_e = 0.3$ and excess losses $K_{ex} = 1.2$ coefficients remain at undamaged values, showing no spatial variation. The reported core-loss values are relative estimates derived from local MOKE loop area and Bertotti-based scaling, rather than direct bulk measurements (e.g., Epstein frame) [19].

Fig. 6 captures the full degradation recovery cycle: at 2 mm from the edge, coercivity and core loss increase by 206% and 103%, while permeability and remanence drop by 82% and 17%. By 12 mm, all parameters recover to within 4%–8% of the reference, validating a 10.6 mm edge exclusion zone for laser-cut 35WW250 laminations. The TD direction consistently shows higher coercivity (+28% over LD at 2 mm), lower initial permeability (−37% vs. LD), reduced remanence (−21% vs. LD), and elevated core loss (+15% vs. LD). These systematic interdirectional differences arise from the preferential 100 easy-axis alignment with the rolling direction in 35WW250 NOES, which renders TD magnetization reversal intrinsically more energetically costly.

IV. Discussion

A. Domain Wall Pinning Mechanisms

The experimental observations presented in Section III can be rationalized within a unified framework of domain wall mechanics [20]. In the annealed, stress-free interior of Sample 1, grain boundaries constitute the primary and relatively sparse

Authorized licensed use limited to: Hebei University of Technology. Downloaded on November 12,2026 at 05:41:56 UTC from IEEE Xplore. Restrictions apply.

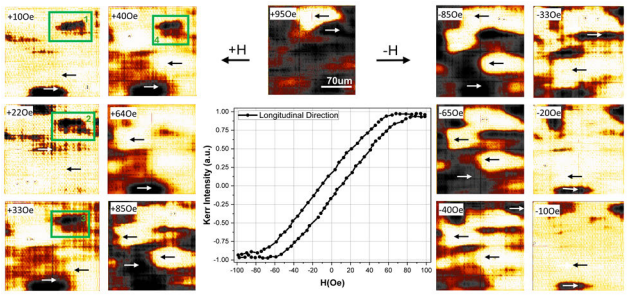


Fig. 8. Domain pattern along the changing magnetic field ±H in the LD near the laser cutting edge (ImageJ rendering).

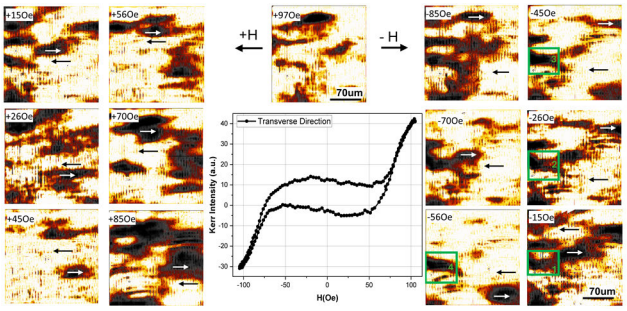


Fig. 9. Domain pattern along the changing magnetic field ±H in the TD near the laser cutting edge (ImageJ rendering).

pinning landscape [21], [22]. Under the applied field, domain walls deform elastically, displaying flexible membrane-like behavior (blue regions, Fig. 7). Figs. 7–9 present domain morphologies alongside their hysteresis loops, with field values labeled on each image to identify the corresponding point on the loop.

The irregular and multidomain patterns near the cut edge (Figs. 8 and 9), contrasted with the symmetric, well-ordered patterns in Fig. 7, provide direct visual confirmation of the pinning driven transition. Green-highlighted regions in Figs. 8 and 9 illustrate domain wall pinning under variable external fields, while the blue-highlighted regions in Fig. 7 show the contrast between rigid (near edge) and flexible (center) wall behavior [23].

While classical pressure models for 180° walls predict a vanishing driving force in the transverse geometry, morphological analysis via Hu invariants reveals a more complex reality. The PCA clustering identifies a transition from mobile, elongated domains in the bulk to rigid, staircase structures near the cut edge. This shift provides a quantitative fingerprint of laser-induced pinning, confirming that the 5.6-fold permeability collapse is driven by structural rigidification rather than simple orientation effects [24]. Fig. 10 shows JA model based estimation of field dependent hysteresis energy while Fig. 11 presents the Hu moment invariant loops extracted from the domain images shown in Figs. 7–9, enabling direct comparison of loop morphologies between the undamaged center and the laser-cut edge.

B. Longitudinal and Transverse MOKE Comparison

The LD and TD MOKE results provide complementary information on magnetization reversal. LD-MOKE mainly reflects the field-parallel response, whereas TD-MOKE is sensitive to transverse magnetization rotation, local anisotropy, and possible 90° domain-wall activity.

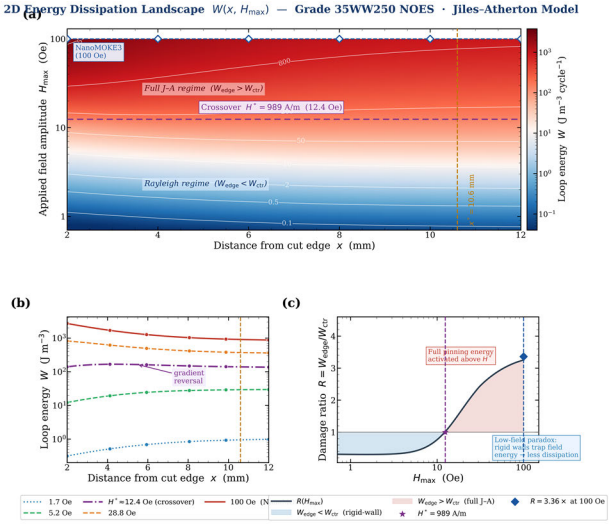


Fig. 10. JA-model-based estimation of field-dependent hysteresis energy. (a) Energy landscape showing the crossover field $H^* = 989\,\mathrm{A/m}\,(12.4\mathrm{Oe})$, where $W_{\mathrm{edge}} = W_{\mathrm{center}}$. (b) Estimated loop energy W as a function of distance from the laser-cut edge for different field amplitudes. (c) Damage ratio $R(H) = W_{\mathrm{edge}}/W_{\mathrm{center}}$, showing that the laser-cut edge becomes more dissipative once the applied field is sufficient to activate irreversible motion across stronger pinning barriers. The values are model-based estimates from local MOKE loops rather than direct bulk core-loss measurements.

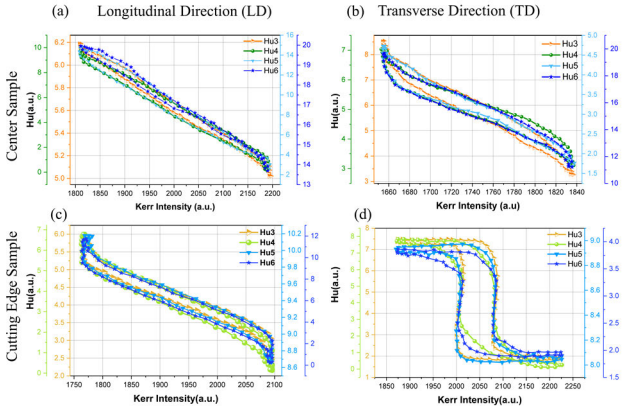


Fig. 11. Evolution of Hu moment invariants (I_3–I_6) as a function of Kerr intensity for (a) and (b) center reference and (c) and (d) laser-cut edge specimens in longitudinal and transverse geometries.

In the center reference sample, LD/TD differences vary from position to position without a systematic trend, indicating natural grain-scale magnetic variability. In contrast, the laser-cut edge sample shows stronger LD/TD separation near $x = 2 - 6$ mm, where the TD response is more distorted than the LD response. This suggests that transverse reversal is more sensitive to laser-induced residual stress and pinning.

As the distance from the cut edge increases, the LD/TD separation decreases, and both responses approach the reference behavior. Therefore, LD-MOKE is used as the primary indicator of field-parallel reversal, while TD-MOKE is used as a complementary indicator of transverse reversal and local anisotropy.

Authorized licensed use limited to: Hebei University of Technology. Downloaded on November 12,2026 at 05:41:56 UTC from IEEE Xplore. Restrictions apply.

C. Role of Rayleigh and JA Modeling

The Rayleigh and JA models were used to interpret the measured loop changes in terms of domain-wall motion and pinning. In the low-field regime, the Rayleigh coefficient α_R describes the irreversible contribution from small domain wall displacement. The increase in α_R near the cut edge is consistent with a more disturbed pinning landscape. The JA model further quantifies this effect through the pinning parameter k_{JA}. The increase of k_{JA} from approximately 250 A/m in the center reference region to 795.5 A/m near the cut edge indicates a higher energy barrier for irreversible domain wall motion.

Therefore, the modeling results support the same physical interpretation obtained from the measured loops and domain images: laser cutting produces a localized pinning-dominated region near the cut edge.

D. Model-Based Crossover Field H^*

The JA analysis identifies a crossover field, $H^* = 989$ A/m (12.4 Oe) in Fig. 10 (below which the laser-damaged edge paradoxically dissipates less energy per cycle than the center). H^* satisfies $W_{edge}(H^*) = W_{center}(H^*)$, where W_{edge} and W_{center} are the loop energies of the edge and center regions, respectively, and W denotes energy dissipated per hysteresis cycle. A physical estimate from the pinning parameters gives

$$H^* \approx k_{JA,edge} + k_{JA,center} = 1045.5A/m \tag{10}$$

where $k_{\mathrm{JA,edge}}$ and $k_{\mathrm{JA,center}}$ are the JA pinning parameters for the laser-cut edge and center reference regions, respectively, within ~6% of the numerical value and confirming consistency with the fit JA parameters.

For $H_{\max} < H^*$, the strongly pinned domain walls near the laser-cut edge undergo limited irreversible displacement with the response dominated by restricted elastic motion. This yields a smaller loop area than in the center region, where lower pinning $\left(k_{\mathrm{JA,center}} | 250\mathrm{A/m}\right)$ allows easier irreversible wall motion. Thus, despite reduced edge permeability, the model predicts lower relative dissipation under low-field excitation.

When $H_{\max} > H^*$, the field overcomes the stronger edge pinning barriers, activating irreversible motion and causing the damage ratio, $R = W_{edge}/W_{center}$ to rise with amplitude, reaching $R = 3.63$ at 100 Oe, as shown in Fig. 10(c). The laser impact is therefore field-dependent: the edge contributes modest additional loss under low fields but becomes strongly dissipative once pinning barriers are fully activated. This interpretation derives from JA-model analysis of local MOKE loops and should not be treated as a direct bulk core-loss measurement.

E. Hu Moment Analysis

The complete seven invariant Hu moment set was computed from binary domain images extracted via Otsu thresholding of NanoMOKE3 Kerr intensity maps. Building on (8) and (9), the invariants encode progressively higher order shape descriptors: I_1 and I_2 capture domain spread and ellipticity; I_3 and I_4 encode third-order boundary asymmetry and triangularity; I_5 and I_6 quantify higher order boundary complexity; and I_7, it is consistent with increasing boundary irregularity and asymmetry associated with pinning-induced domain fragmentation [25], [26]. All invariants are log-transformed as $\hat{I}_k = sign(I_k)\cdot log_{10}(|I_k|)$.

TABLE I

LOG-TRANSFORMED HU MOMENT INVARIANTS ($\hat{I}_k$) REPORTED AS SAMPLE 1 MEAN ± SD (N = 6 POSITIONS ACROSS THE UNDAMAGED SHEET CENTER AND SAMPLE 2 VALUES AT THE TWO DAMAGE EXTREMES (2 MM = PEAK DAMAGE, 12 MM = RECOVERED)

Geometry	Invariant	Sample 1 mean ± SD	Sample 2 at 2 mm	Sample 2 at 12 mm
LD GEOMETRY				
LD	$\hat{I}_1$	-0.739 ± 0.011	**-1.026**	**-0.745**
LD	$\hat{I}_2$	-2.778 ± 0.042	**-3.641**	**-2.797**
LD	$\hat{I}_3$	-4.075 ± 0.073	**-5.188**	**-4.100**
LD	$\hat{I}_4$	-4.501 ± 0.081	**-5.872**	**-4.532**
LD	$\hat{I}_5$	-9.336 ± 0.187	**-11.204**	**-9.378**
LD	$\hat{I}_6$	-6.713 ± 0.134	**-8.459**	**-6.752**
LD	$\hat{I}_7$	-8.921 ± 0.196	**-11.076**	**-8.969**
TD GEOMETRY				
TD	$\hat{I}_1$	-0.751 ± 0.011	**-1.052**	**-0.758**
TD	$\hat{I}_2$	-2.812 ± 0.042	**-3.713**	**-2.832**
TD	$\hat{I}_3$	-4.093 ± 0.074	**-5.510**	**-4.125**
TD	$\hat{I}_4$	-4.519 ± 0.081	**-6.307**	**-4.559**
TD	$\hat{I}_5$	-9.412 ± 0.188	**-11.406**	**-9.457**
TD	$\hat{I}_6$	-6.798 ± 0.136	**-8.610**	**-6.839**
TD	$\hat{I}_7$	-8.867 ± 0.195	**-11.314**	**-8.922**

Notes: Sample 1 was used as the undamaged reference condition. The reported Sample 1 values represent the mean ± standard deviation calculated from six reference measurement positions across the sheet center. The standard deviation reflects natural spatial variability and measurement repeatability of the reference sample. Sample 2 values are reported at $x = 2$ mmand $x = 12$ mmfrom the laser cut edge to represent the maximum-damage and recovered conditions, respectively. Values of $\hat{I}_i$were calculated directly from segmented MOKE domain images after Otsu thresholding. $\hat{I}_7$ is sensitive to asymmetric boundary features; its strong shift at $x = 2$ mm, particularly in TD geometry, indicates enhanced asymmetric domain fragmentation near the laser cut edge.

Characteristic feature vectors confirm pronounced spatial degradation. The undamaged sheet center (Sample 1, LD) yields the reference vector $\hat{I}$ = [−0.739 ± 0.011, −2.778 ± 0.042, −4.075 ± 0.073, −4.501 ± 0.081, −9.336 ± 0.187, −6.713 ± 0.134, −8.921 ± 0.196], with measurement to measurement reproducibility of 1.5%–2.2% of $|\hat{I}_k|$ (n = 6 positions) reflecting geometrically regular,

Authorized licensed use limited to: Hebei University of Technology. Downloaded on November 12,2026 at 05:41:56 UTC from IEEE Xplore. Restrictions apply.

elongated domain morphology consistent with grain-boundary-limited pinning. At the cut edge (Sample 2 at 2 mm, LD), the vector shifts to $\hat{I}$ = [−1.026, −3.641, −5.188, −5.872, −11.204, −8.459, −11.076] every component lying well outside the Sample 1 ±SD envelope (deviations of 4σ to 11σ) with the largest relative changes in $\hat{I}_5$ and $\hat{I}_7$ (−19.9% and −24.2%), quantifying the collapse of higher order boundary complexity at the heat affected interface. In the TD geometry, additional suppression of $\hat{I}_3$ and $\hat{I}_4$ (−27.3% and −30.4% at 2 mm) encodes the loss of rotational symmetry from transverse 90° wall activation. By contrast, Sample 2 at 12 mm exhibits $\hat{I}$ = [−0.745, −2.797, −4.100, −4.532, −9.378, −6.752, −8.969] in LD, with every component recovering to within 1σ of the Sample 1 reference, providing a quantitative morphological confirmation of the 10.6 mm practical damage boundary established from the macroscopic magnetic properties. Full position-wise values and measurement uncertainties are reported in Table I.

Values modeled via exponential decay consistent with β= 0.38 mm^{-1} [(5), $R^2 > 0.97$].

Row Shading Key: Blue = Sample 2 LD; Green = Sample 2 TD.

PCA Summary: PCA was performed on standardized Hu moment features (z-score normalization) from 200 domain images. PC1 (loaded by $\hat{I}_1$, $\hat{I}_2$, $\hat{I}_3$) explains 71.3% of variance; PC2 (loaded by $\hat{I}_7$) explains 15.8%; cumulative = 87.1%.

Fig. 11 presents the evolution of I_3–I_6 as a function of Kerr intensity. For the center sample [Fig. 11(a) and (b)], all four invariants exhibit smooth, monotonically varying trajectories with narrow intermoment separation, confirming geometrically ordered domain structure [27]. The cutting-edge sample [Fig. 11(c) and (d)] displays markedly compressed values, reduced dynamic range, and a pronounced step-like discontinuity in TD geometry. That is a direct morphological signature of avalanche-type domain wall displacements driven by the dense laser-induced pinning landscape. PCA of the full seven-invariant feature matrix yielded PC1 explaining 71.3% of variance (loaded by $\hat{I}_1$, $\hat{I}_2$, $\hat{I}_3$, encoding gross domain size and ellipticity) and PC2 explaining 15.8% (loaded by $\hat{I}_7$, capturing the LD/TD chirality contrast), totaling 87.1% cumulative variance. PC1 scores decrease monotonically from + 2.41 at x = 2 mm to −2.18 at x = 12 mm, tracking the exponential coercivity decay (R^2 = 0.98). K-means clustering (K = 4) identified four domain classes whose area fractions shift from a large stripe-dominant distribution at the center (A_1 = 0.74) to a fragmented domain-dominant distribution at 2 mm (A_3 = 0.58), directly linking domain topology to the observed core loss doubling via the reconstruction weights in (9).

The practical damage zone estimated in this study should be interpreted as a specific value rather than a universal value for laser cutting. The present experiment was performed on 0.35 mm thick 35WW250 NOES using the laser parameters described in Section II. The resulting damage zone length of approximately 10.6 mm reflects this specific combination of material grade, sheet thickness, thermal input, and cutting condition. Other laser systems or optimized cutting parameters may produce a narrower heat-affected zone and a smaller increase in magnetic loss. Therefore, this work should be viewed as a local domain-level case study of laser cutting magnetic degradation, not as a general assessment of all laser punching or cutting technologies.

In this study, no controlled external magnetic field was applied during laser cutting; therefore, the magnetic induction state of the sheet during cutting was not investigated as an independent variable. The observed degradation is mainly attributed to localized thermal effects, rapid cooling, residual stress, and increased domain wall pinning near the cut edge. However, the magnetic state during cutting may influence the final domain configuration through magnetoelastic coupling and stress-assisted domain rearrangement during thermal processing. Future work should therefore examine laser cutting under controlled magnetic bias conditions to determine whether the induction state during cutting affects the final magnetic properties and loss behavior.

V. Conclusion

This study presented a multiscale quantitative investigation of laser cutting-induced magnetic degradation in grade 35WW250 NOES using NanoMOKE3 MOKE magnetometry. Spatial evolution of domain structure and hysteresis morphology was characterized across a 2–12 mm gradient in both longitudinal and transverse geometries, with the complete seven-invariant Hu moment framework combined with PCA (87.1% cumulative variance) providing rotation- and scale-invariant quantitative descriptors of domain topology.

Coercivity peaked at 678 A/m at 2 mm from the cut edge, a 206% increase over the undamaged reference (222 A/m), consistent with the exponential decay model (β = 0.38 mm^{-1}, $R^2 > 0.97$). The domain-wall pinning coefficient increased by a factor of 3.18 fold (from 250 to 795 A/m), initial permeability decreased by a factor of 5.6 fold and remanence was reduced by 17% (TD). Concurrently, total core loss nearly doubled (from 13,674 to 27,704 W/m^3); this increase was attributable solely to the hysteresis component, as eddy-current and excess losses remained spatially invariant. A crossover field $H^* \approx$ 989 A/m was identified, below which rigid cut edge walls dissipate less energy than the undamaged interior, confirming that cutting induced penalties are negligible under low flux no-load conditions and become significant only near rated flux density. All parameters recovered to within 4%–8% of reference values at 12 mm, establishing a practical 10.6 mm heat affected zone exclusion boundary. This value should be regarded as condition specific rather than universal, since the damage-zone length and loss increase may vary significantly with laser power, cutting speed, beam condition, thermal input, sheet thickness, and material grade.

The consistent TD anisotropy across all positions confirms that laser damage amplifies the intrinsic 100 easy-axis texture rather than selectively degrading one direction. Future work should extend this framework to variable laser parameters for process property mapping, incorporate EBSD to correlate grain boundary density with the pinning gradient, and apply the Hu moment pipeline to mechanical punching and wire EDM for a unified cutting damage assessment protocol.

Acknowledgment

This work was supported by the National Natural Science Foundation of China under Grant 52277008 and Grant 52130710.

Authorized licensed use limited to: Hebei University of Technology. Downloaded on November 12,2026 at 05:41:56 UTC from IEEE Xplore. Restrictions apply.

REFERENCES

[1] Y. Fu and L. Li, "Modeling and analysis of stress sensitivity and changing trend of magnetization characteristics of GO silicon steel cut along different angles to the rolling direction," *IEEE Trans. Magn.*, vol. 60, no. 3, pp. 1–5, Mar. 2024, doi: 10.1109/TMAG.2023.3313991.

[2] Z. Gmyrek and A. Cavagnino, "Analytical model of the ferromagnetic properties in laminations damaged by cutting," in *Proc. IEEE Energy Convers. Congr. Expo. (ECCE)*, Oct. 2021, pp. 4000–4007, doi: 10.1109/ECCE47101.2021.9595736.

[3] Z. Gmyrek, F. Graffeo, S. Vaschetto, and A. Cavagnino, "Measurements and modeling of iron losses in guillotine and laser cut soft-magnetic sheets," *IEEE Open J. Ind. Appl.*, vol. 6, pp. 663–675, 2025, doi: 10.1109/OJIA.2025.3607115.

[4] Z. Guo, B. H. Nguyen, H. Hamzehbahmani, and R. V. Sabariego, "Dynamic hysteresis model of grain-oriented ferromagnetic material using neural operators," *IEEE Trans. Magn.*, vol. 61, no. 10, pp. 1–7, Oct. 2025, doi: 10.1109/TMAG.2025.3600089.

[5] M. Cossale, M. Kitzberger, G. Goldbeck, G. Bramerdorfer, D. Andessner, and W. Amrhein, "Local degradation in soft magnetic materials: A simplified modeling approach," *IEEE Trans. Ind. Appl.*, vol. 55, no. 6, pp. 5897–5905, Nov. 2019, doi: 10.1109/TIA.2019.2940918.

[6] M. Dems, K. Komeza, and J. Szulakowski, "Practical approximation of sheet losses taking into account the guillotine and laser cutting effect," *Energies*, vol. 16, no. 6, p. 2831, Mar. 2023, doi: 10.3390/en16062831.

[7] I. T. Gürbüz et al., "Experimental characterization of the effect of uniaxial stress on magnetization and iron losses of electrical steel sheets cut by punching process," *J. Magn. Magn. Mater.*, vol. 549, May 2022, Art. no. 168983, doi: 10.1016/j.jmmm.2021.168983.

[8] C. Zhang, X. Yan, Y. Li, and Q. Yang, "Vector magnetic properties measurement of silicon steel under biased magnetic excitation along laminated direction," *IEEE Trans. Magn.*, vol. 55, no. 2, pp. 1–4, Feb. 2019.

[9] L. Boehm et al., "Grain size influence on the magnetic property deterioration of blanked non-oriented electrical steels," *Materials*, vol. 14, no. 22, p. 7055, Nov. 2021, doi: 10.3390/ma14227055.

[10] M. Dems, Z. Gmyrek, and K. Komeza, "The influence of cutting technology on magnetic properties of non-oriented electrical steel—Review state of the art," *Energies*, vol. 16, no. 11, p. 4299, May 2023, doi: 10.3390/en16114299.

[11] D. Ma, C. Sun, Y. Li, B. Tian, L. Wang, and R. Pei, "Study of magnetic properties of electrical steels with different Si content considering the effect of temperature," *AIP Adv.*, vol. 13, no. 2, Feb. 2023, Art. no. 2, doi: 10.1063/9.0000578.

[12] A. Selema, M. N. Ibrahim, and P. Sergeant, "Non-destructive electromagnetic evaluation of material degradation due to steel cutting in a fully stacked electrical machine," *Energies*, vol. 15, no. 21, p. 7862, Oct. 2022, doi: 10.3390/en15217862.

[13] F. Wu, L. Zhou, S. Juliette, and C. Davis, "Effect of plastic damage orientation with respect to the magnetic flux pathway on the magnetic properties in ngo electrical steel for electric motors," *Tech. Rep.*, Jan. 2023, doi: 10.2139/ssrn.4492336. [Online]. Available: https://papers.ssrn.com/sol3/papers.cfm?abstract_id=4492336

[14] R. Shahbaz, C. Zhang, H. Fatima, H. Zhang, and Y. Zhang, "Quantifying magnetic degradation in laser-cut electrical steel: A domain-level study with angle-dependent magnetization," *AIP Adv.*, vol. 16, no. 2, Feb. 2026, Art. no. 025124, doi: 10.1063/9.0000978.

[15] F. M. Bayer, D. M. Bayer, A. Marinoni, and P. Gamba, "A novel Rayleigh dynamical model for remote sensing data interpretation," *IEEE Trans. Geosci. Remote Sens.*, vol. 58, no. 7, pp. 4989–4999, Jul. 2020, doi: 10.1109/TGRS.2020.2971345.

[16] V. Kvasnička, "Construction of model Hamiltonians in framework of Rayleigh–Schrödinger perturbation theory," *Czechoslovak J. Phys.*, vol. 24, no. 6, pp. 605–615, Jun. 1974, doi: 10.1007/bf01587295.

[17] I. T. Gürbüz et al., "Finite-element modeling and characterization of iron losses in 12 mm thick steel laminations including the effect of cutting," *IEEE Access*, vol. 9, pp. 115710–115718, 2021, doi: 10.1109/ACCESS.2021.3105909.

[18] J. L. García-Palacios and F. J. Lázaro, "Langevin-dynamics study of the dynamical properties of small magnetic particles," *Phys. Rev. B, Condens. Matter*, vol. 58, no. 22, pp. 14937–14958, Dec. 1998, doi: 10.1103/physrevb.58.14937.

[19] C. Zhang, G. Sun, and Z. Lin, "Analysis of magnetic domain evolution in rotational magnetization of GOES based on morphological characteristics and artificial neural network," *J. Magn. Magn. Mater.*, vol. 630, Oct. 2025, Art. no. 173415.

[20] D. Ma, C. Sun, B. Tian, L. Zeng, and R. Pei, "Effect of cutting process on the magnetic properties of electrical steels with different si contents," *IEEE Trans. Magn.*, vol. 60, no. 9, pp. 1–5, Sep. 2024, doi: 10.1109/TMAG.2024.3401119.

[21] D. Ma et al., "Analysis and calculation of iron loss in electrical motors with high silicon steel considering multi-physics coupling," *IEEE Trans. Energy Convers.*, vol. 40, no. 3, pp. 1946–1958, Sep. 2025, doi: 10.1109/TEC.2025.3552424.

[22] H. Wang, J. Chen, and Y. Jiang, "Effect of cutting methods on magnetic properties of non-oriented silicon steel lamination," *IEEE Trans. Appl. Supercond.*, vol. 34, no. 8, pp. 1–5, Nov. 2024, doi: 10.1109/TASC.2024.3425277.

[23] S. Honda, H. Itoh, and Y. Sonobe, "Multi-bit magnetic memory based on domain wall motion in a vertical nanopillar with two perpendicularly magnetized pinning layers," *IEEE Trans. Magn.*, vol. 62, no. 3, pp. 1–5, Mar. 2026, doi: 10.1109/TMAG.2025.3611334.

[24] H. Naumoski et al., "Magneto-optical and field-metric evaluation of the punching effect on magnetic properties of electrical steels with varying alloying content and grain size," *Tech. Rep.*, Dec. 2014, pp. 1–9, doi: 10.1109/edpc.2014.6984398.

[25] D. Ma et al., "Effect of Si content on magnetostrictive properties of electrical steel sheet considering tensile stress," *IEEE Trans. Magn.*, vol. 60, no. 9, pp. 1–5, Sep. 2024, doi: 10.1109/TMAG.2024.3408219.

[26] M. N. Rohman et al., "Prediction and optimization of geometrical quality for pulsed laser cutting of non-oriented electrical steel sheet," *Opt. Laser Technol.*, vol. 149, May 2022, Art. no. 107847, doi: 10.1016/j.optlastec.2022.107847.

[27] C. Zhang, Y. Zhang, Y. Li, and Q. Yang, "Magnetic properties deterioration of non-oriented steel due to laser cutting," *AIP Adv.*, vol. 13, 2023, Art. no. 025360, doi: 10.1063/9.0000586.

Authorized licensed use limited to: Hebei University of Technology. Downloaded on November 12,2026 at 05:41:56 UTC from IEEE Xplore. Restrictions apply.